

Charm- and bottom-quark production in Au+Au collisions at $\sqrt{s} = 200$ GeV

(PHENIX Collaboration) Abdulameer, N. J.; Acharya, U.; Adare, A.; Aidala, C.; Ajitanand, N. N.; Akiba, Y.; Alfred, M.; Apadula, N.; Asano, H.; Azmoun, B.; ...

Source / Izvornik: **Physical Review C, 2024, 109**

Journal article, Published version

Rad u časopisu, Objavljena verzija rada (izdavačev PDF)

<https://doi.org/10.1103/PhysRevC.109.044907>

Permanent link / Trajna poveznica: <https://urn.nsk.hr/urn:nbn:hr:217:181036>

Rights / Prava: [In copyright](#) / [Zaštićeno autorskim pravom](#).

Download date / Datum preuzimanja: **2024-10-19**



Repository / Repozitorij:

[Repository of the Faculty of Science - University of Zagreb](#)



Charm- and bottom-quark production in Au+Au collisions at $\sqrt{s_{NN}} = 200$ GeV

N. J. Abdulameer,¹⁵ U. Acharya,²⁰ A. Adare,¹² C. Aidala,⁴² N. N. Ajitanand,^{61,*} Y. Akiba,^{56,57,†} M. Alfred,²² N. Apadula,^{27,62} H. Asano,^{34,56} B. Azmoun,⁷ V. Babintsev,²³ M. Bai,⁶ N. S. Bandara,⁴⁰ B. Bannier,⁶² K. N. Barish,⁸ S. Bathe,^{5,57} A. Bazilevsky,⁷ M. Beaumier,⁸ S. Beckman,¹² R. Belmont,^{12,42,49} A. Berdnikov,⁵⁹ Y. Berdnikov,⁵⁹ L. Bichon,⁶⁷ B. Blankenship,⁶⁷ D. S. Blau,^{33,46} J. S. Bok,⁴⁸ V. Borisov,⁵⁹ K. Boyle,⁵⁷ M. L. Brooks,³⁶ J. Bryslawskij,^{5,8} V. Bumazhnov,²³ S. Campbell,^{13,27} V. Canoa Roman,⁶² C.-H. Chen,⁵⁷ M. Chiu,⁷ C. Y. Chi,¹³ I. J. Choi,²⁴ J. B. Choi,^{29,*} T. Chujo,⁶⁶ Z. Citron,⁶⁸ M. Connors,²⁰ R. Corliss,⁶² Y. Corrales Morales,³⁶ M. Csanád,¹⁶ T. Csörgő,^{41,69} T. W. Danley,⁵⁰ A. Datta,⁴⁷ M. S. Daugherty,¹ G. David,^{7,62} C. T. Dean,³⁶ K. DeBlasio,⁴⁷ K. Dehmelt,⁶² A. Denisov,²³ A. Deshpande,^{57,62} E. J. Desmond,⁷ A. Dion,⁶² P. B. Diss,³⁹ J. H. Do,⁷⁰ V. Doomra,⁶² A. Drees,⁶² K. A. Drees,⁶ J. M. Durham,³⁶ A. Durum,²³ A. Enokizono,^{56,58} R. Esha,⁶² B. Fadem,⁴⁴ W. Fan,⁶² N. Feege,⁶² D. E. Fields,⁴⁷ M. Finger, Jr.,⁹ M. Finger,⁹ D. Firak,^{15,62} D. Fitzgerald,⁴² S. L. Fokin,³³ J. E. Frantz,⁵⁰ A. Franz,⁷ A. D. Frawley,¹⁹ P. Gallus,¹⁴ C. Gal,⁶² P. Garg,^{3,62} H. Ge,⁶² M. Giles,⁶² F. Giordano,²⁴ A. Glenn,³⁵ Y. Goto,^{56,57} N. Grau,² S. V. Greene,⁶⁷ M. Grosse Perdekamp,²⁴ T. Gunji,¹¹ T. Hachiya,^{45,56,57} J. S. Haggerty,⁷ K. I. Hahn,¹⁷ H. Hamagaki,¹¹ H. F. Hamilton,¹ J. Hanks,⁶² S. Y. Han,^{17,32} M. Harvey,⁶⁴ S. Hasegawa,²⁸ T. O. S. Haseler,²⁰ K. Hashimoto,^{56,58} T. K. Hemmick,⁶² X. He,²⁰ J. C. Hill,²⁷ A. Hodges,^{20,24} R. S. Hollis,⁸ K. Homma,²¹ B. Hong,³² T. Hoshino,²¹ N. Hotvedt,²⁷ J. Huang,⁷ K. Imai,²⁸ M. Inaba,⁶⁶ A. Iordanova,⁸ D. Isenhower,¹ D. Ivanishchev,⁵⁴ B. V. Jacak,⁶² M. Jezzghani,²⁰ X. Jiang,³⁶ Z. Ji,⁶² B. M. Johnson,^{7,20} D. Jouan,⁵² D. S. Jumper,²⁴ S. Kanda,¹¹ J. H. Kang,⁷⁰ D. Kawall,⁴⁰ A. V. Kazantsev,³³ J. A. Key,⁴⁷ V. Khachatryan,⁶² A. Khanzadeev,⁵⁴ A. Khatiwada,³⁶ B. Kimelman,⁴⁴ C. Kim,³² D. J. Kim,³⁰ E.-J. Kim,²⁹ G. W. Kim,¹⁷ M. Kim,⁶⁰ T. Kim,¹⁷ D. Kincses,¹⁶ A. Kingan,⁶² E. Kistenev,⁷ R. Kitamura,¹¹ J. Klatsky,¹⁹ D. Kleinjan,⁸ P. Kline,⁶² T. Koblesky,¹² B. Komkov,⁵⁴ D. Kotov,^{54,59} L. Kovacs,¹⁶ B. Kurgyis,^{16,62} K. Kurita,⁵⁸ M. Kurosawa,^{56,57} Y. Kwon,⁷⁰ J. G. Lajoie,²⁷ D. Larionova,⁵⁹ A. Lebedev,²⁷ S. Lee,⁷⁰ S. H. Lee,^{27,42,62} M. J. Leitch,³⁶ N. A. Lewis,⁴² S. H. Lim,^{55,70} M. X. Liu,³⁶ X. Li,¹⁰ X. Li,³⁶ D. A. Loomis,⁴² D. Lynch,⁷ S. Lökös,¹⁶ T. Majoros,¹⁵ Y. I. Makdisi,⁶ M. Makek,⁷¹ A. Manion,⁶² V. I. Manko,³³ E. Mannel,⁷ M. McCumber,³⁶ P. L. McGaughey,³⁶ D. McGlinchey,^{12,36} C. McKinney,²⁴ A. Meles,⁴⁸ M. Mendoza,⁸ A. C. Mignerey,³⁹ A. Milov,⁶⁸ D. K. Mishra,⁴ J. T. Mitchell,⁷ M. Mitrankova,⁵⁹ Iu. Mitrankov,⁵⁹ S. Miyasaka,^{56,65} S. Mizuno,^{56,66} A. K. Mohanty,⁴ M. M. Mondal,⁶² P. Montuenga,²⁴ T. Moon,^{32,70} D. P. Morrison,⁷ T. V. Moukhanova,³³ A. Muhammad,⁴³ B. Mulilo,^{32,56,72} T. Murakami,^{34,56} J. Murata,^{56,58} A. Mwai,⁶¹ K. Nagashima,²¹ J. L. Nagle,¹² M. I. Nagy,¹⁶ I. Nakagawa,^{56,57} H. Nakagomi,^{56,66} K. Nakano,^{56,65} C. Nattrass,⁶³ S. Nelson,¹⁸ P. K. Netrakanti,⁴ T. Niida,⁶⁶ S. Nishimura,¹¹ R. Nouicer,^{7,57} N. Novitzky,^{30,62,66} T. Novák,^{41,69} G. Nukazuka,^{56,57} A. S. Nyanin,³³ E. O'Brien,⁷ C. A. Ogilvie,²⁷ J. Oh,⁵⁵ J. D. Orjuela Koop,¹² M. Orosz,¹⁵ J. D. Osborn,^{7,42,51} A. Oskarsson,³⁷ K. Ozawa,^{31,66} R. Pak,⁷ V. Pantuev,²⁵ V. Papavassiliou,⁴⁸ J. S. Park,⁶⁰ S. Park,^{43,56,60,62} M. Patel,²⁷ S. F. Pate,⁴⁸ J.-C. Peng,²⁴ W. Peng,⁶⁷ D. V. Perepelitsa,^{7,12} G. D. N. Perera,⁴⁸ D. Yu. Peressounko,³³ C. E. PerezLara,⁶² J. Perry,²⁷ R. Petti,^{7,62} C. Pinkenburg,⁷ R. Pinson,¹ R. P. Pisani,⁷ M. Potekhin,⁷ A. Pun,⁵⁰ M. L. Purschke,⁷ P. V. Radzevich,⁵⁹ J. Rak,³⁰ N. Ramasubramanian,⁶² B. J. Ramson,⁴² I. Ravinovich,⁶⁸ K. F. Read,^{51,63} D. Reynolds,⁶¹ V. Riabov,^{46,54} Y. Riabov,^{54,59} D. Richford,⁵ T. Rinn,^{24,27} S. D. Rolnick,⁸ M. Rosati,²⁷ Z. Rowan,⁵ J. G. Rubin,⁴² J. Runchey,²⁷ B. Sahlmueller,⁶² N. Saito,³¹ T. Sakaguchi,⁷ H. Sako,²⁸ V. Samsonov,^{46,54} M. Sarsour,²⁰ S. Sato,²⁸ B. Schaefer,⁶⁷ B. K. Schmoll,⁶³ K. Sedgwick,⁸ R. Seidl,^{56,57} A. Sen,^{27,63} R. Seto,⁸ P. Sett,⁴ A. Sexton,³⁹ D. Sharma,⁶² I. Shein,²³ M. Shibata,⁴⁵ T.-A. Shibata,^{56,65} K. Shigaki,²¹ M. Shimomura,^{27,45} Z. Shi,³⁶ P. Shukla,⁴ A. Sickles,^{7,24} C. L. Silva,³⁶ D. Silvermyr,^{37,51} B. K. Singh,³ C. P. Singh,³ V. Singh,³ M. Slunečka,⁹ K. L. Smith,¹⁹ M. Snowball,³⁶ R. A. Soltz,³⁵ W. E. Sondheim,³⁶ S. P. Sorensen,⁶³ I. V. Sourikova,⁷ P. W. Stankus,⁵¹ M. Stepanov,^{40,*} S. P. Stoll,⁷ T. Sugitate,²¹ A. Sukhanov,⁷ T. Sumita,⁵⁶ J. Sun,⁶² Z. Sun,¹⁵ J. Sziklai,⁶⁹ R. Takahama,⁴⁵ A. Taketani,^{56,57} K. Tanida,^{28,57,60} M. J. Tannenbaum,⁷ S. Tarafdar,^{67,68} A. Taranenko,^{46,61} R. Tieulent,^{20,38} A. Timilsina,²⁷ T. Todoroki,^{56,57,66} M. Tomášek,¹⁴ C. L. Towell,¹ R. Towell,¹ R. S. Towell,¹ I. Tserruya,⁶⁸ Y. Ueda,²¹ B. Ujvari,¹⁵ H. W. van Hecke,³⁶ J. Velkovska,⁶⁷ M. Virius,¹⁴ V. Vrba,^{14,26} X. R. Wang,^{48,57} Z. Wang,⁵ Y. Watanabe,^{56,57} Y. S. Watanabe,^{11,31} F. Wei,⁴⁸ A. S. White,⁴² C. P. Wong,^{20,36} C. L. Woody,⁷ M. Wysocki,⁵¹ B. Xia,⁵⁰ L. Xue,²⁰ S. Yalcin,⁶² Y. L. Yamaguchi,^{11,62} A. Yanovich,²³ I. Yoon,⁶⁰ J. H. Yoo,³² I. E. Yushmanov,³³ H. Yu,^{48,53} W. A. Zajc,¹³ A. Zelenski,⁶ S. Zhou,¹⁰ and L. Zou⁸

(PHENIX Collaboration)

¹Abilene Christian University, Abilene, Texas 79699, USA²Department of Physics, Augustana University, Sioux Falls, South Dakota 57197, USA³Department of Physics, Banaras Hindu University, Varanasi 221005, India⁴Bhabha Atomic Research Centre, Bombay 400 085, India⁵Baruch College, City University of New York, New York, New York 10010, USA⁶Collider-Accelerator Department, Brookhaven National Laboratory, Upton, New York 11973-5000, USA⁷Physics Department, Brookhaven National Laboratory, Upton, New York 11973-5000, USA

*Deceased.

†PHENIX Spokesperson: akiba@rcf.rhic.bnl.gov

- ⁸University of California-Riverside, Riverside, California 92521, USA
- ⁹Charles University, Faculty of Mathematics and Physics, 180 00 Troja, Prague, Czech Republic
- ¹⁰Science and Technology on Nuclear Data Laboratory, China Institute of Atomic Energy, Beijing 102413, People's Republic of China
- ¹¹Center for Nuclear Study, Graduate School of Science, University of Tokyo, 7-3-1 Hongo, Bunkyo, Tokyo 113-0033, Japan
- ¹²University of Colorado, Boulder, Colorado 80309, USA
- ¹³Columbia University, New York, New York 10027 and Nevis Laboratories, Irvington, New York 10533, USA
- ¹⁴Czech Technical University, Zikova 4, 166 36 Prague 6, Czech Republic
- ¹⁵Debrecen University, H-4010 Debrecen, Egyetem tér 1, Hungary
- ¹⁶ELTE, Eötvös Loránd University, H-1117 Budapest, Pázmány P. s. 1/A, Hungary
- ¹⁷Ewha Womans University, Seoul 120-750, Korea
- ¹⁸Florida A&M University, Tallahassee, Florida 32307, USA
- ¹⁹Florida State University, Tallahassee, Florida 32306, USA
- ²⁰Georgia State University, Atlanta, Georgia 30303, USA
- ²¹Physics Program and International Institute for Sustainability with Knotted Chiral Meta Matter (SKCM2), Hiroshima University, Higashi-Hiroshima, Hiroshima 739-8526, Japan
- ²²Department of Physics and Astronomy, Howard University, Washington, DC 20059, USA
- ²³IHEP Protvino, State Research Center of Russian Federation, Institute for High Energy Physics, Protvino 142281, Russia
- ²⁴University of Illinois at Urbana-Champaign, Urbana, Illinois 61801, USA
- ²⁵Institute for Nuclear Research of the Russian Academy of Sciences, prospekt 60-letiya Oktyabrya 7a, Moscow 117312, Russia
- ²⁶Institute of Physics, Academy of Sciences of the Czech Republic, Na Slovance 2, 182 21 Prague 8, Czech Republic
- ²⁷Iowa State University, Ames, Iowa 50011, USA
- ²⁸Advanced Science Research Center, Japan Atomic Energy Agency, 2-4 Shirakata Shirane, Tokai-mura, Naka-gun, Ibaraki-ken 319-1195, Japan
- ²⁹Jeonbuk National University, Jeonju, 54896, Korea
- ³⁰Helsinki Institute of Physics and University of Jyväskylä, P.O.Box 35, FI-40014 Jyväskylä, Finland
- ³¹KEK, High Energy Accelerator Research Organization, Tsukuba, Ibaraki 305-0801, Japan
- ³²Korea University, Seoul 02841, Korea
- ³³National Research Center "Kurchatov Institute", Moscow, 123098 Russia
- ³⁴Kyoto University, Kyoto 606-8502, Japan
- ³⁵Lawrence Livermore National Laboratory, Livermore, California 94550, USA
- ³⁶Los Alamos National Laboratory, Los Alamos, New Mexico 87545, USA
- ³⁷Department of Physics, Lund University, Box 118, SE-221 00 Lund, Sweden
- ³⁸IPNL, CNRS/IN2P3, Université Lyon 1, F-69622, Villeurbanne, France
- ³⁹University of Maryland, College Park, Maryland 20742, USA
- ⁴⁰Department of Physics, University of Massachusetts, Amherst, Massachusetts 01003-9337, USA
- ⁴¹MATE, Laboratory of Femtoscopy, Károly Róbert Campus, H-3200 Gyöngyös, Mátraiút 36, Hungary
- ⁴²Department of Physics, University of Michigan, Ann Arbor, Michigan 48109-1040, USA
- ⁴³Mississippi State University, Mississippi State, Mississippi 39762, USA
- ⁴⁴Muhlenberg College, Allentown, Pennsylvania 18104-5586, USA
- ⁴⁵Nara Women's University, Kita-uoya Nishi-machi Nara 630-8506, Japan
- ⁴⁶National Research Nuclear University, MEPhI, Moscow Engineering Physics Institute, Moscow 115409, Russia
- ⁴⁷University of New Mexico, Albuquerque, New Mexico 87131, USA
- ⁴⁸New Mexico State University, Las Cruces, New Mexico 88003, USA
- ⁴⁹Physics and Astronomy Department, University of North Carolina at Greensboro, Greensboro, North Carolina 27412, USA
- ⁵⁰Department of Physics and Astronomy, Ohio University, Athens, Ohio 45701, USA
- ⁵¹Oak Ridge National Laboratory, Oak Ridge, Tennessee 37831, USA
- ⁵²IPN-Orsay, Université Paris-Sud, CNRS/IN2P3, Université Paris-Saclay, BPI, F-91406, Orsay, France
- ⁵³Peking University, Beijing 100871, People's Republic of China
- ⁵⁴PNPI, Petersburg Nuclear Physics Institute, Gatchina, Leningrad region, 188300, Russia
- ⁵⁵Pusan National University, Pusan 46241, Korea
- ⁵⁶RIKEN Nishina Center for Accelerator-Based Science, Wako, Saitama 351-0198, Japan
- ⁵⁷RIKEN BNL Research Center, Brookhaven National Laboratory, Upton, New York 11973-5000, USA
- ⁵⁸Physics Department, Rikkyo University, 3-34-1 Nishi-Ikebukuro, Toshima, Tokyo 171-8501, Japan
- ⁵⁹Saint Petersburg State Polytechnic University, St. Petersburg, 195251 Russia
- ⁶⁰Department of Physics and Astronomy, Seoul National University, Seoul 151-742, Korea
- ⁶¹Chemistry Department, Stony Brook University, SUNY, Stony Brook, New York 11794-3400, USA
- ⁶²Department of Physics and Astronomy, Stony Brook University, SUNY, Stony Brook, New York 11794-3800, USA
- ⁶³University of Tennessee, Knoxville, Tennessee 37996, USA
- ⁶⁴Texas Southern University, Houston, Texas 77004, USA

⁶⁵*Department of Physics, Tokyo Institute of Technology, Oh-okayama, Meguro, Tokyo 152-8551, Japan*

⁶⁶*Tomonaga Center for the History of the Universe, University of Tsukuba, Tsukuba, Ibaraki 305, Japan*

⁶⁷*Vanderbilt University, Nashville, Tennessee 37235, USA*

⁶⁸*Weizmann Institute, Rehovot 76100, Israel*

⁶⁹*Institute for Particle and Nuclear Physics, Wigner Research Centre for Physics, Hungarian Academy of Sciences (Wigner RCP, RMKI) H-1525 Budapest 114, POBox 49, Budapest, Hungary*

⁷⁰*Yonsei University, IPAP, Seoul 120-749, Korea*

⁷¹*Department of Physics, Faculty of Science, University of Zagreb, Bijenička c. 32 HR-10002 Zagreb, Croatia*

⁷²*Department of Physics, School of Natural Sciences, University of Zambia, Great East Road Campus, Box 32379, Lusaka, Zambia*



(Received 5 April 2022; revised 31 January 2024; accepted 23 February 2024; published 10 April 2024)

The invariant yield of electrons from open-heavy-flavor decays for $1 < p_T < 8$ GeV/ c at midrapidity $|y| < 0.35$ in Au+Au collisions at $\sqrt{s_{NN}} = 200$ GeV has been measured by the PHENIX experiment at the BNL Relativistic Heavy Ion Collider. A displaced-vertex analysis with the PHENIX silicon-vertex detector enables extraction of the fraction of charm and bottom hadron decays and unfolding of the invariant yield of parent charm and bottom hadrons. The nuclear-modification factors R_{AA} for electrons from charm and bottom hadron decays and heavy-flavor hadrons show both a centrality and a quark-mass dependence, indicating suppression in the quark-gluon plasma produced in these collisions that is medium sized and quark-mass dependent.

DOI: [10.1103/PhysRevC.109.044907](https://doi.org/10.1103/PhysRevC.109.044907)

I. INTRODUCTION

Charm (c) and bottom (b) quarks, with masses of $m_c \approx 1.3$ GeV/ c^2 and $m_b \approx 4.2$ GeV/ c^2 , are much heavier than the temperature reached in the quark-gluon plasma (QGP) produced at the BNL Relativistic Heavy Ion Collider (RHIC) and the CERN Large Hadron Collider (LHC). As such, charm and bottom quarks, collectively known as heavy-flavor quarks, are produced predominantly at the primordial stages of high-energy nucleus-nucleus collisions and negligibly via interactions between thermalized particles in the QGP. Once produced, heavy quarks lose energy while propagating through the QGP and, for that reason, open-heavy-flavor hadrons are excellent probes of the properties of the QGP. The current status of both experimental and theoretical developments is reviewed in Ref. [1].

Experiments at RHIC and the LHC have measured the cross section of inclusive heavy flavor, as well as those for charm and bottom separated final states [2–11]. Previous measurements of separated charm and bottom heavy-flavor cross sections at RHIC, obtained in minimum-bias (MB) Au+Au collisions at $\sqrt{s_{NN}} = 200$ GeV by the PHENIX Collaboration, suggest lower suppression of electrons from bottom hadron decays $b \rightarrow e$ compared to those from charm-hadron decays ($c \rightarrow e$) in the range of $3 < p_T < 4$ GeV/ c [12]. This is in agreement with the widely postulated mass ordering for energy loss by quarks (q) and gluons (g) in the QGP, $\Delta E_g > \Delta E_{u,d,s} > \Delta E_c > \Delta E_b$ at $p_T > 4$ GeV/ c . Due to the large systematic uncertainties on the $p + p$ baseline measurement, the nuclear-modification factor R_{AA} did not definitively constrain the suppression pattern and mass dependence of the energy-loss mechanism.

Although heavy-flavor hadron-production mechanisms have been studied widely, the mechanisms that contribute to the in-medium modification thereof are not well understood. Many classes of models exist that employ one or more of the following effects: radiative energy loss [13,14], collisional

energy loss [15], or dissociation and coalescence [16] of heavy-flavor hadrons in the medium. While radiative energy loss is significant at high p_T ($> \approx 10$ GeV/ c), theoretical models suggest that collisional energy loss is equally important at low p_T [16]. Cold-nuclear-matter effects, such as the Cronin effect for heavy quarks, could also play an important role in the interpretation of these observations at low to medium p_T [17]. For these reasons, a precise measurement of the nuclear-modification factor R_{AA} over a broad range of momentum and centrality is necessary to investigate the interplay between competing mechanisms that could contribute to the suppression or enhancement seen in different regions of phase space.

This paper reports on the measurement of electrons from semileptonic decays of open charm and bottom hadrons at midrapidity $|y| < 0.35$ in Au+Au collisions at $\sqrt{s_{NN}} = 200$ GeV. Using the combination of the high-statistics data set recorded in 2014 and the updated $p + p$ reference from 2015 [18], nuclear-modification factors R_{AA} of separated charm and bottom electrons in MB Au+Au as well as four centrality classes in Au+Au can be measured with improved precision compared to our previously published results [12].

This paper is organized as follows. Section II provides a brief introduction to the PHENIX detector, with special emphasis on the central arm detectors pertinent to this measurement. Section III details track reconstruction, electron identification, event selection, background estimation, signal extraction, and unfolding. Section IV describes systematic-uncertainty estimates. Section V provides the results of the measurement, along with comparisons with theoretical models. Finally, Sec. VI gives the summary and conclusions.

II. EXPERIMENTAL SETUP

PHENIX has previously published the decay-electron contribution from charm and bottom decays separately [12,18]

through the combination of electron-identification detectors in the central arms covering $|y| < 0.35$, and the measurement of event-vertex and decay-electron trajectories provided by an inner silicon tracker (VTX). The detector systems relevant to this measurement are discussed below, while a detailed description of the PHENIX detector is given in Refs. [19–21].

The VTX is described in detail in Refs. [18,22]. It is composed of two arms, each with $|\eta| < 1$ and $\Delta\phi \approx 0.8\pi$ coverage. Each arm has four layers around the beam pipe. The radial distances of these layers from the nominal beam center are 2.6, 5.1, 11.8, and 16.7 cm. The innermost two layers have pixel segmentation of $50 \times 425 \mu\text{m}$. The two outer layers have strip segmentation of $80 \times 1000 \mu\text{m}$.

III. ANALYSIS METHOD

This paper reports measurements using data collected by the PHENIX experiment during the 2014 high-luminosity Au+Au collisions at $\sqrt{s_{NN}} = 200 \text{ GeV}$. The data were recorded with a MB trigger and correspond to an integrated luminosity of 2.3 nb^{-1} . A set of event, offline track, and electron selection cuts were applied as described below.

A. Event selection

Events considered here are characterized by the MB trigger, which requires simultaneous activity in both beam-beam-counter (BBC) phototube arrays located at pseudorapidity $3.0 < |\eta| < 3.9$ and the zero-degree calorimeter at 18 m downstream from the intersection point. This criterion selects $93 \pm 2\%$ of the Au+Au inelastic cross section. The total number of charged particles as measured by the BBC determines the collision centrality. The BBC is also used later to calculate the number of nucleon participants and the number of binary collisions via comparisons with Monte Carlo Glauber model simulations of the collisions [23]. The results shown here are for MB Au+Au collisions and 0%–10%, 10%–20%, 20%–40%, and 40%–60% centrality classes.

The collision vertex is determined by clusters of converging VTX tracks. The vertex resolution is determined from the standard deviation of the difference between the vertex position measured by each VTX at the east and west arm. The vertex resolutions for $x - y - z$ coordinate are $(\sigma_x, \sigma_y, \sigma_z) = (44, 38, 48) \mu\text{m}$. The radial beam profile during the 2014 run had a width of $45 \mu\text{m}$ and was very stable during beam fills. The beam-center position in the xy plane was then determined from the average position during the fill to avoid autocorrelations between the vertex determination and the distance of closest approach (DCA) measurements in each event. Because of the modest RHIC collision rates in 2014 of less than 10 kHz in Au+Au collisions, no significant contributions were found of multiple collisions per beam crossing or signal pileup in the dataset. The analysis required a z vertex within $\pm 10 \text{ cm}$ reconstructed by the VTX detector.

B. Track reconstruction

Charged-particle tracks are reconstructed (trajectory and momentum) by the PHENIX central-arm drift chambers (DC)

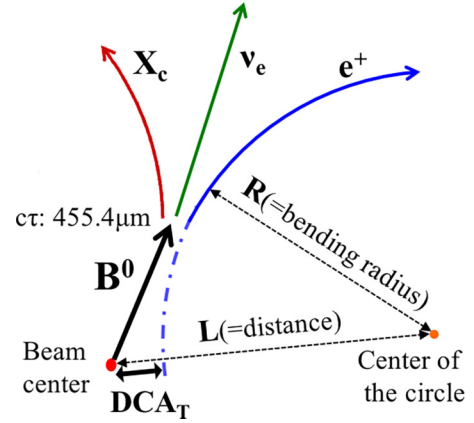


FIG. 1. Definition of the distance of the closest approach DCA_T in the transverse plane (normal to the beam direction).

and pad chambers covering the pseudorapidity $|\eta| < 0.35$ and azimuthal angle $\Delta\phi = \pi/2$. To identify electrons and positrons, the reconstructed tracks are projected to the ring-imaging Čerenkov detector (RICH). Electrons and positrons are collectively referred to here as electrons. In the momentum range where charged pions are below the RICH radiator threshold ($p_T < 4.7 \text{ GeV}/c$), tracks are required to be associated with signals in two phototubes within a radius expected of electron Čerenkov rings. Above this threshold, to aid in eliminating pion background, associated signals in three phototubes are required. Additional tracking information is provided by pad chambers that are immediately behind the RICH.

Energy-momentum matching is also required for electron identification. Electromagnetic calorimeters (EMCal) are the outermost detectors in the PHENIX central arms. The EMCal comprises eight sectors, two of which are lead-glass layers, and six of which are lead-scintillator layers. Tracks with measured momentum p that are associated with showers in the calorimeters of energy E are characterized by the variable $\text{dep} = (E/p - \mu_{E/p})/\sigma_{E/p}$, where $\mu_{E/p}$ and $\sigma_{E/p}$ are the mean and standard deviation of a precalibrated Gaussian E/p distribution. The requirement of $\text{dep} > -2$ further removes background from hadron tracks associated with Čerenkov rings produced by nearby electrons or high-momentum pions. Remaining background contributions are quantified as discussed below.

The reconstructed tracks are then associated to VTX hits to perform the displaced tracking around the collision vertex. Taking advantage of the different decay lengths of charm and bottom hadrons (viz. for D^0 the decay length is $c\tau = 122.9 \mu\text{m}$ and for the B^0 it is $c\tau = 455.4 \mu\text{m}$ [24]), electrons from these decays are statistically separated based on the DCA_T in the transverse plane ($x-y$, normal to the beam direction) to the collision vertex. Figure 1 illustrates the definition of $\text{DCA}_T = L - R$ for a VTX-associated track, where R is a radius of the circle defined by the track trajectory in the constant magnetic field around the VTX region and L is the length between the beam center and the center of the circle.

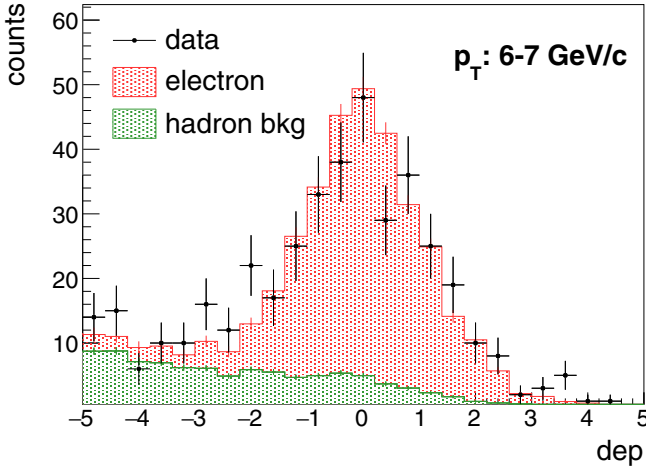


FIG. 2. A fit result of the **dep** distribution for electron candidates with $p_T = 6-7$ GeV/ c in MB Au+Au collisions. The red and green distributions are the estimated contributions for electrons and hadron backgrounds.

C. Background estimation

1. Misreconstruction

In a high-multiplicity environment, tracks are accidentally reconstructed with hits from different particles. Misreconstructed tracks have two sources: (i) misidentified hadrons composed of tracks accidentally matching RICH Čerenkov rings or EMCal clusters; and (ii) mismatches between DC tracks and uncorrelated VTX hits.

The misidentified hadron-track contamination is estimated with a sample of tracks where the sign of their z direction is swapped. The swapped tracks that, after being projected to RICH, match Čerenkov rings provides the expected number of misidentified hadrons. Charged hadrons with momentum $p > 4.7$ GeV/ c also radiate Čerenkov light and make RICH hits, meaning the swap method underestimates the fraction of misidentified hadrons. The contamination at high p_T is estimated by the **dep** template method, in which the measured **dep** distribution is assumed to be the sum of the electron distribution and the hadron-background distribution. The **dep** template for the electron distribution is obtained by the RICH swap method for $p_T \leq 4.5$ GeV/ c , where the hadron contamination is very small. The **dep** template for hadron backgrounds is obtained by vetoing the electron candidates from all reconstructed tracks. The measured **dep** distribution for $p_T > 4.5$ GeV/ c is fitted with the electron and hadron background templates. An example of the **dep** template method is shown in Fig. 2 for electron candidates at $6 < p_T < 7$ GeV/ c in MB Au+Au collisions. The electron signal in the **dep** distribution is centered at **dep** = 0. The background tail due to hadrons overlaps the signal region. The hadron background increases at higher p_T .

The mismatch between DC tracks and uncorrelated VTX hits is estimated by the VTX swap method, which intentionally creates a mismatch by changing the angle of DC tracks by 10 degrees in the ϕ - η plane. The 10-degree rotation is sufficiently larger than the angular resolution of the DC such

that the rotated tracks are never connected with VTX hits belonging to the same particle.

2. Photonic background

Photonic electrons are the main background source in this analysis. They are produced by internal conversions (Dalitz decay) and photon conversions at the beam pipe and the first VTX layer. Photonic conversions produced in the other layers of the VTX do not produce tracks accepted by the tracking algorithm because the presence of a hit in the first layer is required. Electron pairs from converted photons have a small opening angle, therefore it is required that an electron track should not have a neighboring electron track with $-0.02 < \text{chrg} \times \Delta\phi < 0.04$ radian for $p_T < 1.8$ GeV/ c and narrower for high p_T , where chrg is the charge of the track and $\Delta\phi$ is the azimuthal difference of electron pairs. This isolation cut minimizes the contamination from internal and external conversion electrons, and is the same as described in Ref. [12].

The number of electrons obtained after removing background from misidentified and mismatched tracks but before the isolation cut, (N_e), is the sum of photonic (N_P) and non-photonic sources (N_{NP}):

$$N_e = N_P + N_{NP}, \quad (1)$$

while the number of electrons after the isolation cut is

$$\tilde{N}_e = \varepsilon_P \times \varepsilon_{UC} \times N_P + \varepsilon_{UC} \times N_{NP}, \quad (2)$$

where ε_P is the survival rate after the isolation cut for the correlated pairs such as photonic electrons, and ε_{UC} is the survival rate for the uncorrelated tracks. The ε_{UC} is also applied to both the photonic and nonphotonic electrons because uncorrelated tracks appear everywhere. By solving Eqs. (1) and (2) simultaneously, N_P and N_{NP} are described as

$$N_P = \frac{\tilde{N}_e - N_e \varepsilon_{UC}}{\varepsilon_{UC}(\varepsilon_P - 1)} \quad (3)$$

and

$$N_{NP} = \frac{N_e \varepsilon_P \varepsilon_{UC} - \tilde{N}_e}{\varepsilon_{UC}(\varepsilon_P - 1)}. \quad (4)$$

The fraction of photonic and nonphotonic electrons is then written as

$$F_P = \frac{\varepsilon_P \varepsilon_{UC} N_P}{\varepsilon_P \varepsilon_{UC} N_P + \varepsilon_{UC} N_{NP}} \quad (5)$$

and

$$F_{NP} = \frac{\varepsilon_{UC} N_{NP}}{\varepsilon_P \varepsilon_{UC} N_P + \varepsilon_{UC} N_{NP}}. \quad (6)$$

Figure 3 shows F_{NP} as a function of p_T for MB Au+Au collisions as well as four centrality classes, which correspond to 0%–10%, 10%–20%, 20%–40%, and 40%–60%. The F_{NP} values increase with p_T and their curves are similar for all centrality classes.

3. Nonphotonic background

Nonphotonic background sources are electrons from the three-body decays of kaons and the decay of J/ψ and Υ . The other contributions from the resonance decays of ρ , ω , ϕ , and

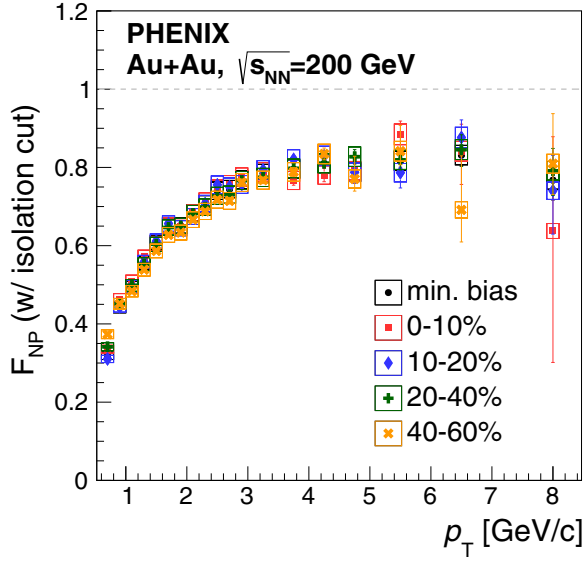


FIG. 3. The fraction of nonphotonic electrons (F_{NP}) as a function of p_T for MB and the indicated four centrality classes.

the Drell-Yan process are found to be negligibly small compared to the total background. The nonphotonic backgrounds included in F_{NP} are estimated by the full GEANT-3 simulation of the PHENIX detector with measured particle yields [25,26] as inputs and normalized by the background cocktail, applying with the uncorrelated survival rate ε_{UC} . The detailed modeling of these backgrounds is described in Ref. [12]. After subtracting these backgrounds, the remaining signal component is the inclusive heavy flavor (F_{c+b}). Figure 4 shows the fractions of signal, photonic, and nonphotonic backgrounds of isolated electrons in MB Au+Au collisions.

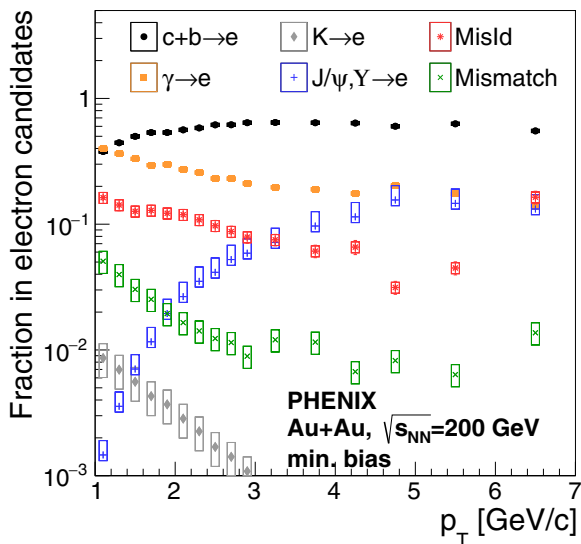


FIG. 4. The fractions of signal component in isolated electron-track candidates as a function of p_T in MB Au+Au collisions. The isolation cut is applied. The modeling of these backgrounds is described in the text and in Ref. [12].

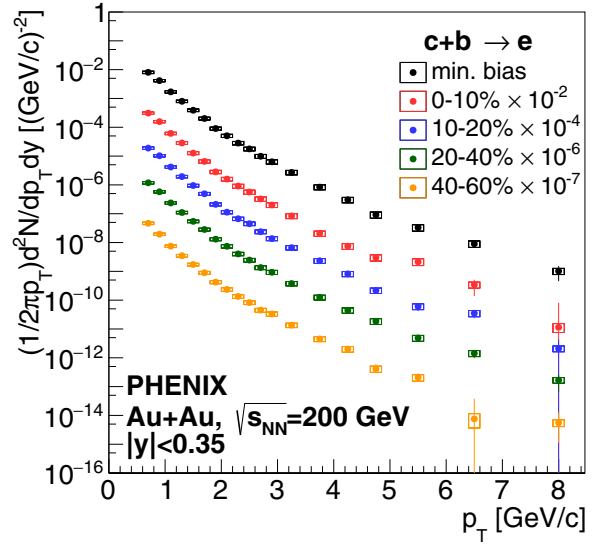


FIG. 5. The invariant yields of $c + b \rightarrow e$ as a function of p_T for different Au+Au centrality classes. These spectra are scaled by factors of 10 for clarity.

D. Invariant yields of heavy-flavor electrons

The invariant yield of heavy-flavor electrons is calculated from the photonic electron yields and the fraction of heavy-flavor electrons to photonic electrons as

$$\frac{d^2 N_e^{c+b}}{dp_T dy} = \frac{d^2 N_e^{c+b} (N_e^\gamma)}{dp_T dy} \times \frac{F_{c+b}}{F_P}, \quad (7)$$

where N_e^{c+b} (N_e^γ), F_{c+b} (F_P), and $d^2 N_e^\gamma / dp_T dy$ are the yield, fraction, and invariant yield, respectively, of heavy-flavor (photonic) electrons. The photonic electron yield is calculated based on the invariant yields of π^0 and η measured by PHENIX [27,28], using a method which has been demonstrated to give an accurate description of photonic electron yields in the previous heavy-flavor electron measurement [12,29]. The fractions F_{c+b} and F_P are determined by the data-driven method described in the previous section. Note that the efficiency and acceptance cancel out in F_{c+b} and F_P . The invariant yields of heavy-flavor electrons ($c + b \rightarrow e$) in MB Au+Au as well as four centrality classes in Au+Au are shown in Fig. 5. The bars and boxes represent statistical and systematic uncertainties which are described in Sec. IV.

E. DCA_T distribution of the background

The DCA_T distribution of misidentified hadrons and mismatched backgrounds are determined by the RICH and VTX swap method as described in Sec. III C 1. The swap method is data driven and the obtained DCA_T distribution includes the normalization and resolution effects. Photonic- and nonphotonic-background DCA_T distributions are determined by the full GEANT-3 simulation of the PHENIX detector. Background sources are generated with the p_T distribution measured by PHENIX and decay electron tracks are reconstructed and analyzed with the same analysis cuts used to calculate DCA_T . The obtained DCA_T distributions are

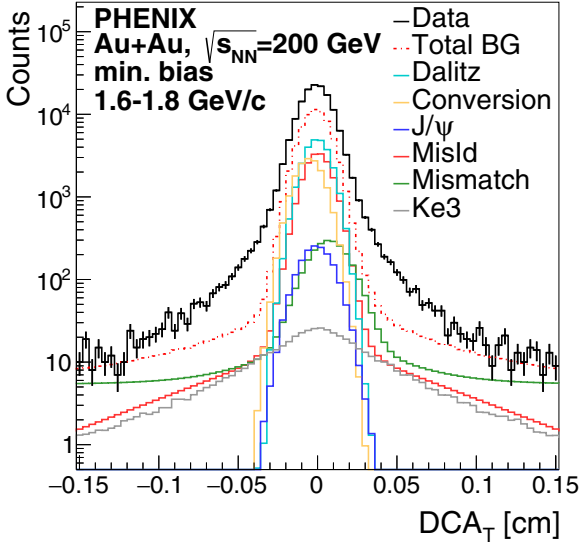


FIG. 6. DCA_T distribution of electron candidates for $1.6 < p_T < 1.8$ GeV/c in MB collisions. All background components are also plotted.

fitted with Gaussian functions for photonic, J/ψ , and Υ backgrounds, and Laplace functions for kaon backgrounds to obtain smooth shapes. These DCA_T distributions are normalized by the factors described in the previous section (Sec. III C 1).

The DCA_T resolution of the data and the Monte Carlo simulation are compared. The resolution of the DCA_T distribution is a convolution of the position resolution of the VTX and the beam spot size. The simulation was generated with ideal VTX geometry and a single beam-spot-size value and smeared to correct for differences with the real data caused by irreducible misalignments including the time dependence of the beam spot size during data taking. The smearing is calculated as a function of p_T by comparing the DCA_T width of charged hadrons between data and simulation. The smearing is independent of the collision centrality because DCA_T is measured from the beam center.

Figure 6 shows the smeared and normalized DCA_T distributions for these background sources. Most of the background sources are primary particles showing up in the DCA_T distributions as Gaussian shapes. Kaon-decay electrons as well as misidentified and mismatched backgrounds have large DCA_T tails. Misidentified hadrons contain long-lived hadrons such as Λ particles causing large DCA_T tails. Mismatch tracks also cause large tails in the DCA_T distribution because they are formed by hits from different particles.

E. Unfolding

Because the p_T spectra and decay lengths of charm and bottom hadrons are significantly different, simultaneous fits to the p_T and DCA_T distributions of heavy-flavor electrons enable separation of $c \rightarrow e$ and $b \rightarrow e$ components. However, the p_T and DCA_T template distributions for $c \rightarrow e$ and $b \rightarrow e$ depend on unmeasured p_T spectra of the parent charm and bottom hadrons. To solve this inverse problem and to measure

the hadron yields, the decay of heavy-flavor hadrons into final-state electrons is characterized by using a Bayesian-inference unfolding method that was also used by PHENIX in previous publications [12, 18].

This unfolding procedure is a likelihood-based approach that uses the Markov-chain Monte Carlo (MCMC) algorithm [30] to sample the parameter space and maximize the joint posterior probability distribution. The response matrix or decay matrix assigns a probability for a hadron at given p_T^h to decay into an electron with p_T^e and DCA_T . The yields of charm and bottom hadrons with 17 p_T bins each within $0 < p_T^h < 20$ GeV/c are set as unfolding parameters.

The PYTHIA6 generator¹ [31] is used to model the decay matrix, which includes charm ($D^0, D^\pm, D_s, \Lambda_c$), and bottom hadrons ($B^0, B^\pm, B_s, \Lambda_b$) from the whole rapidity range decaying into electrons within $|y| < 0.35$. The relative contributions of the charm hadrons and bottom hadrons are modeled by PYTHIA. Thus, the decay matrix has some model dependence which may affect the final results.

In the decay matrix, there are two assumptions. One is that the rapidity distributions of hadrons are not changed in $A + A$ collisions. The BRAHMS collaboration reported [32] that the nuclear modification of pions and protons at $y \approx 3$ is similar to that at midrapidity. The rapidity modification is also less sensitive to the final result because electron contributions from large rapidity to the PHENIX acceptance with $|y| < 0.35$ are small. The second assumption is that the relative contributions of charm (bottom) hadrons are unchanged. The charm hadrons have their own decay lengths which can affect the final results. Charm-baryon enhancement in Au+Au collisions was reported by the STAR collaboration [33]. To study the effect of this, the baryon enhancement for charm and bottom hadrons was tested using a modified decay matrix [34]. Following Ref. [35], the baryon enhancement for charm and bottom is assumed to be the same as that for strange hadrons. The result is that baryon enhancement produces a lower charm-hadron yield and a higher bottom-hadron yield at high p_T , but the difference is within the systematic uncertainties discussed in the next section. The test result is not included in the final result.

In each sampling step, a set of hadron yields are selected by the MCMC algorithm. The p_T and DCA_T distributions in the decay-electron space are predicted by applying corresponding decay matrices to the sampled values. The predicted p_T and DCA_T distributions along with the measured ones are used to compute a log-likelihood:

$$\ln \mathcal{L} = \ln P(\mathbf{Y}^{\text{data}} | \mathbf{Y}(\boldsymbol{\theta})) + \sum_{j=1}^{12} \ln P(\mathbf{D}_j^{\text{data}} | \mathbf{D}_j(\boldsymbol{\theta})), \quad (8)$$

where \mathbf{Y}^{data} and $\mathbf{D}_j^{\text{data}}$ represent a vector of measured p_T and 12 vectors of measured DCA_T in the range of 1.0–8.0 and

¹Using PYTHIA6.2 with CTEQ5L parton distribution function, the following parameters were modified: MSEL=5, MSTP(91)=1, PARP(91)=1.5, MSTP(33)=1, PARP(31)=2.5. For bottom (charm) hadron studies, PARJ(13)=0.75(0.63), PARJ(2)=0.29(0.2), PARJ(1)=0.35(0.15).

1.6–6.0 GeV/ c , respectively. For the 40%–60% centrality bin, 11 vectors of measured DCA_T in 1.6–5.0 GeV/ c are used due to statistical limitations. The $Y(\theta)$ and $D(\theta)_j$ represent the p_T and DCA_T distribution predicted by the unfolding procedure. MCMC repeats the process through multiple iterations until an optimal solution is found. Only statistical uncertainties in the data are included in the calculation of the log-likelihood.

The analyzing power to separate charm and bottom contributions is mainly contained in the tail of the DCA_T distribution, but the DCA_T distribution has a sharp peak with many measurements at $DCA_T = 0$, which dominates the likelihood calculation in the unfolding method. A 5% uncertainty is added in quadrature to the statistical uncertainty when a given DCA_T bin has a yield above a threshold that was set to 100.

Without additional information, the unfolding procedure introduces large statistical fluctuations in the unfolded distributions due to negative correlations of adjacent bins. However, the unknown hadron spectra are expected to be relatively smooth. This prior belief of smoothness, π , is multiplied with the likelihood to get a posterior distribution P as

$$\ln \pi(\theta) = -\alpha^2(|\mathbf{LR}_c|^2 + |\mathbf{LR}_b|^2) \quad (9)$$

and

$$\ln P = \ln \mathcal{L} + \ln \pi(\theta), \quad (10)$$

where \mathbf{L} denotes a 17×17 matrix of regularization conditions and, $\mathbf{R}_b(\mathbf{R}_c)$ is the ratio of the trial bottom (charm) spectra to the prior. The strength of regularization is characterized using a parameter α that is tuned by repeating the unfolding procedure with several values of α and selecting the one that gives a maximum of the posterior distribution.

Once the unfolded charm- and bottom-hadron p_T spectra are obtained, the same response matrices are applied to the heavy-flavor hadron distribution to obtain refolded $c + b \rightarrow e$ yields. Figure 7 shows the refolded invariant yield of $c + b \rightarrow e$ compared to the measured data, which is in reasonable agreement with the refolded spectrum. Figure 8 compares the refolded DCA_T distributions to the measured data. The DCA_T distribution is fit with the refolded components within $|DCA_T| < 0.1$ cm, and indicates good agreement between the measured and refolded distributions.

IV. SYSTEMATIC UNCERTAINTIES

The systematic uncertainties are independently evaluated for the measured data and the unfolding procedure. Figure 9 shows the contribution of each systematic uncertainty source. The total uncertainty is obtained by adding them in quadrature. Each source of uncertainty is discussed below.

1. Background normalization

Systematic uncertainties associated with modeling of the background processes are estimated from the difference between the nominal measurement and that obtained by repeating the unfolding procedure with systematic variation of the background DCA_T normalization. The background DCA_T template for each source of background is modified independently by $\pm 1\sigma$ of the nominal value, and the unfolding

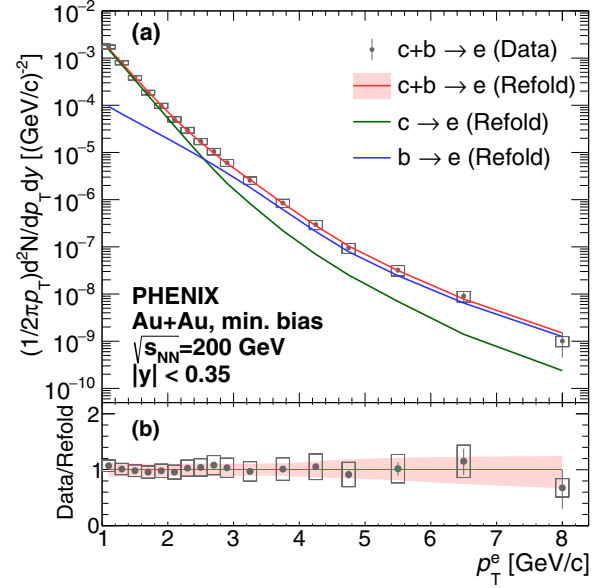


FIG. 7. The measured invariant yield for (black markers) $c + b \rightarrow e$ as a function of p_T and refolded yields for (red line) $c + b \rightarrow e$, (green line) $c \rightarrow e$, and (blue line) $b \rightarrow e$ in MB Au+Au collisions.

procedure is repeated with the modified-background DCA_T template. For each background source, the difference between the unfolding result using nominal-background templates and that with a modified-background template is taken as the systematic uncertainty. Estimates of background normalization uncertainty from all the background processes are added in quadrature to get a single value of the background normalization uncertainty.

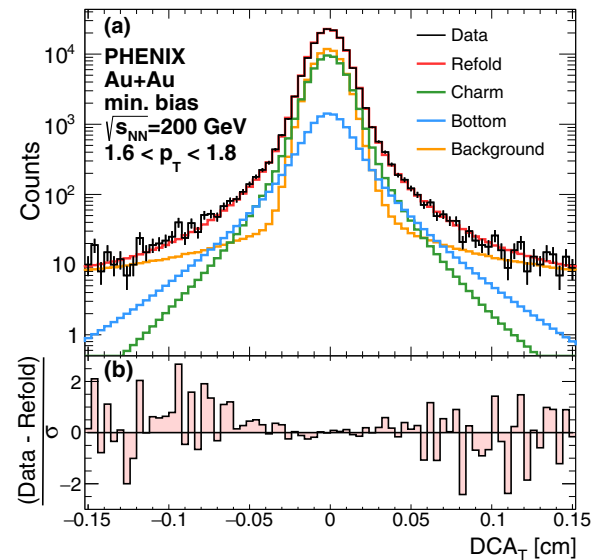


FIG. 8. The measured DCA_T distribution of (black line) electron tracks, (red line) refolded $c + b \rightarrow e$, (yellow line) background, (green line) $c \rightarrow e$, and (blue line) $b \rightarrow e$ in MB Au+Au collisions for $1.6 < p_T < 1.8$ GeV/ c .

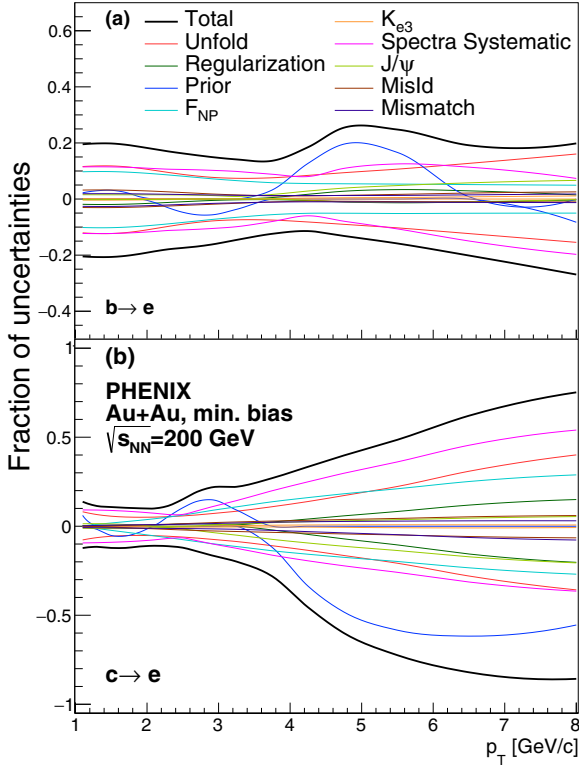


FIG. 9. The fractions of each systematic uncertainty in the invariant yield of (a) $b \rightarrow e$ and (b) $c \rightarrow e$ (in MB Au+Au collisions).

2. Measured yield of $c + b \rightarrow e$

The unfolding procedure only considers statistical uncertainty on the measured yield of $c + b \rightarrow e$ in the log-likelihood calculation. The systematic uncertainty on the measured yield of $c + b \rightarrow e$ needs to be accounted for separately. To calculate the systematic uncertainty, an input p_T spectrum is modified by either kinking or tilting the spectrum. Tilting implies modifying the spectrum by pivoting the nominal spectrum about a given point such that the lowest p_T point goes up by the systematic uncertainty and the highest p_T point goes down by the same systematic uncertainty, while the intermediate points are modified with the linear interpolation of the two points. In contrast, kinking implies that the modified spectrum is folded based on the nominal spectrum. The control point for both tilting and kinking is chosen at $p_T = 1.8$ or 5.0 GeV/ c because analysis cuts are changed at these points. Once the spectra are modified with this tilting and kinking method, the unfolding procedure is run with eight modified spectra, and the root mean square of the difference from the nominal result is assigned as a systematic uncertainty.

3. Choice of prior

In the Bayesian approach to unfolding, the prior is chosen to reflect a priori knowledge of model parameters. In this analysis, PYTHIA-based distributions are used to model this initial knowledge. In theory, the optimal distributions obtained through the iterative unfolding procedure should be

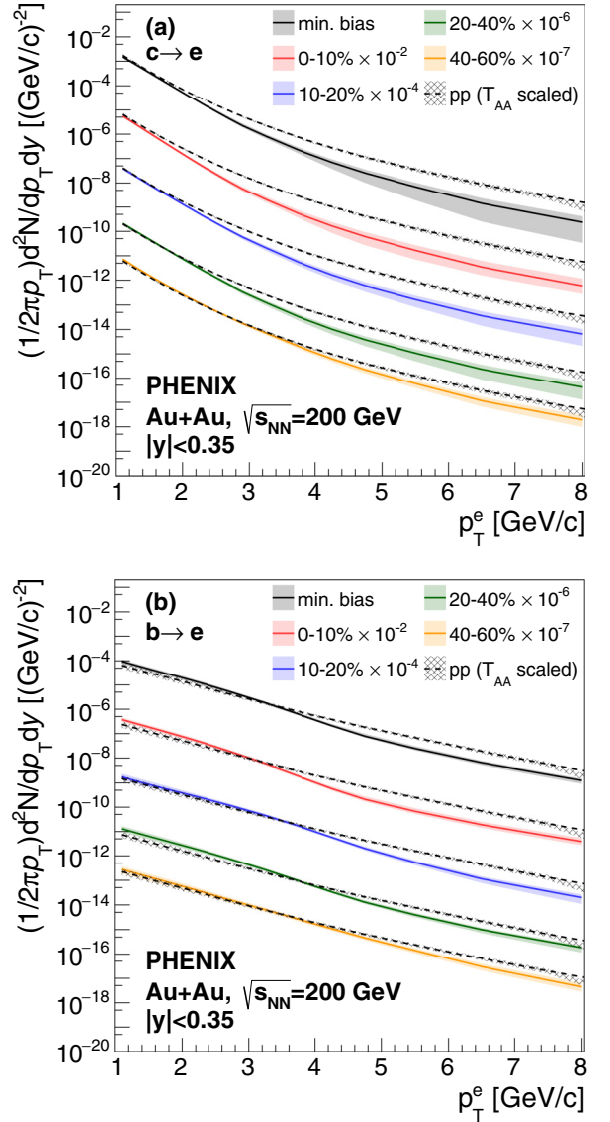


FIG. 10. Comparison of refolded p_T spectrum of (a) $c \rightarrow e$ and (b) $b \rightarrow e$ in Au+Au collisions to that scaled by T_{AA} in $p + p$ collisions [18].

independent of the choice of the prior. However, residual model dependencies could be present. To account for any uncertainties due to the choice of the prior, the unfolding procedure is repeated with a modified prior, and the difference in the unfolded result from the nominal is assigned as a systematic uncertainty. The modified PYTHIA spectra are obtained by scaling heavy-flavor-hadron yields in PYTHIA with the blast-wave model [37].

4. Regularization hyperparameter

We control the strength of the regularization (spectrum smoothness) with a hyperparameter α of Eq. (9). The uncertainty due to α is determined by changing α by a half unit of the maximum-likelihood value which corresponds to 1σ deviation. The differences of the unfolded results with these α values are taken as the systematic uncertainty of α .

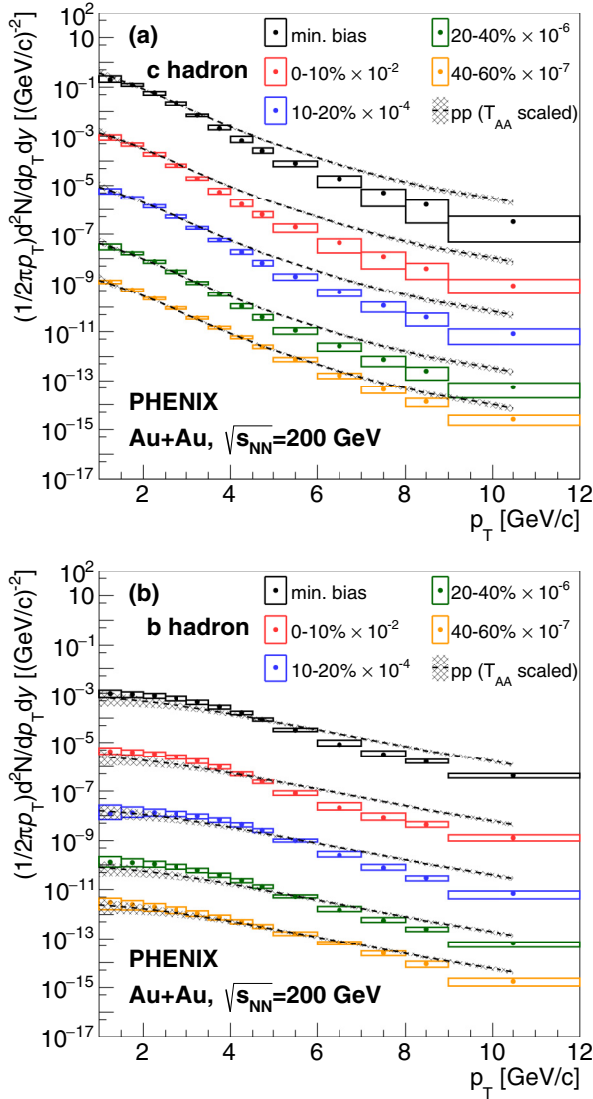


FIG. 11. Comparison of unfolded p_T spectrum of (a) charm hadrons and (b) bottom hadrons in Au+Au collisions to that scaled by T_{AA} in $p + p$ collisions [18].

V. RESULTS

A. Invariant yield

The Bayesian unfolding is applied for MB Au+Au collisions as well as four centrality classes in Au+Au collisions. Figure 10 shows the invariant yields of electrons from charm and bottom hadron decays in Au+Au collisions at $\sqrt{s} = 200$ GeV. The line represents the median of the yield distribution at a given p_T and the band represents the 1σ limits on the point-to-point correlated uncertainty. These yields are compared with the PHENIX $p + p$ result scaled by the nuclear-overlap function, T_{AA} [18]. Both comparisons of the invariant yields of $c \rightarrow e$ and $b \rightarrow e$ show substantial yield suppression at high p_T . The suppression increases at higher p_T and in more-central collisions.

The invariant yields of charm and bottom hadrons are unfolded point-by-point in 17 bins for each centrality class as

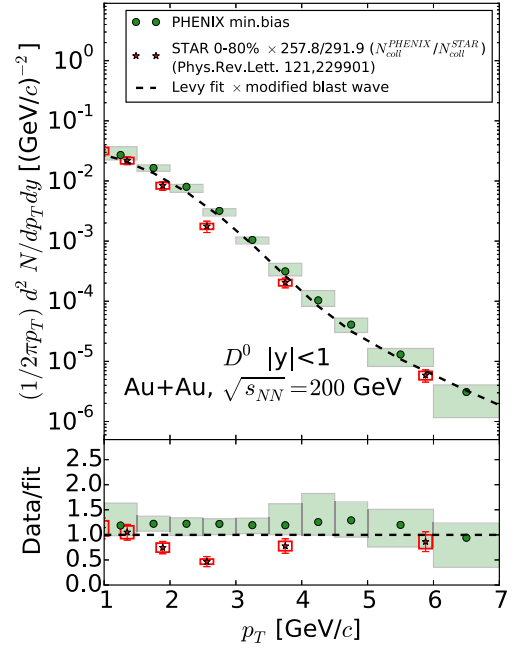


FIG. 12. Unfolded yield of D^0 mesons as a function of p_T at midrapidity $|y| < 1$, compared to the measurement from STAR [36].

shown in Fig. 11. The point at each p_T bin is the most likely value of the hadron yields to describe the measured electron yields and DCA_T distributions. Note that the hadron yields are integrated over all rapidity because the decay matrix used in the unfolding method handles all hadron rapidity decaying into electrons in the PHENIX acceptance.

Our unfolded charm-hadron yields have been compared with D^0 yields in Au+Au collisions measured by the STAR collaboration [36]. To compare them, PYTHIA is used to calculate the D^0 fraction within $|y| < 1$ compared to all charm hadrons for the whole rapidity region. To match the centrality range, the STAR result is scaled by the ratio of the number of binary collisions. This comparison is shown in Fig. 12. For clarity, we have fit our unfolded D^0 yields with the modified Levy function used in Ref. [12]. The ratio of the data to the fit is shown in the bottom panel of Fig. 12. Within uncertainties, the unfolded D^0 yield is found to be in qualitative agreement with the D^0 yields [36].

B. Nuclear modification factor R_{AA} vs. p_T

To compare the yield suppression between charm and bottom quarks, the nuclear-modification factor R_{AA} is calculated as

$$R_{AA}^{c \rightarrow e} = \frac{(1 - F_{AuAu})}{(1 - F_{pp})} R_{AA}^{HF}, \quad (11)$$

$$R_{AA}^{b \rightarrow e} = \frac{F_{AuAu}}{F_{pp}} R_{AA}^{HF}, \quad (12)$$

where F_{AuAu} (F_{pp}) is the bottom electron fraction in Au+Au ($p + p$), and R_{AA}^{HF} is the nuclear modification of inclusive heavy-flavor electrons (charm and bottom) whose yields are fully anticorrelated. The $R_{AA}^{c \rightarrow e}$ and $R_{AA}^{b \rightarrow e}$ are calculated by

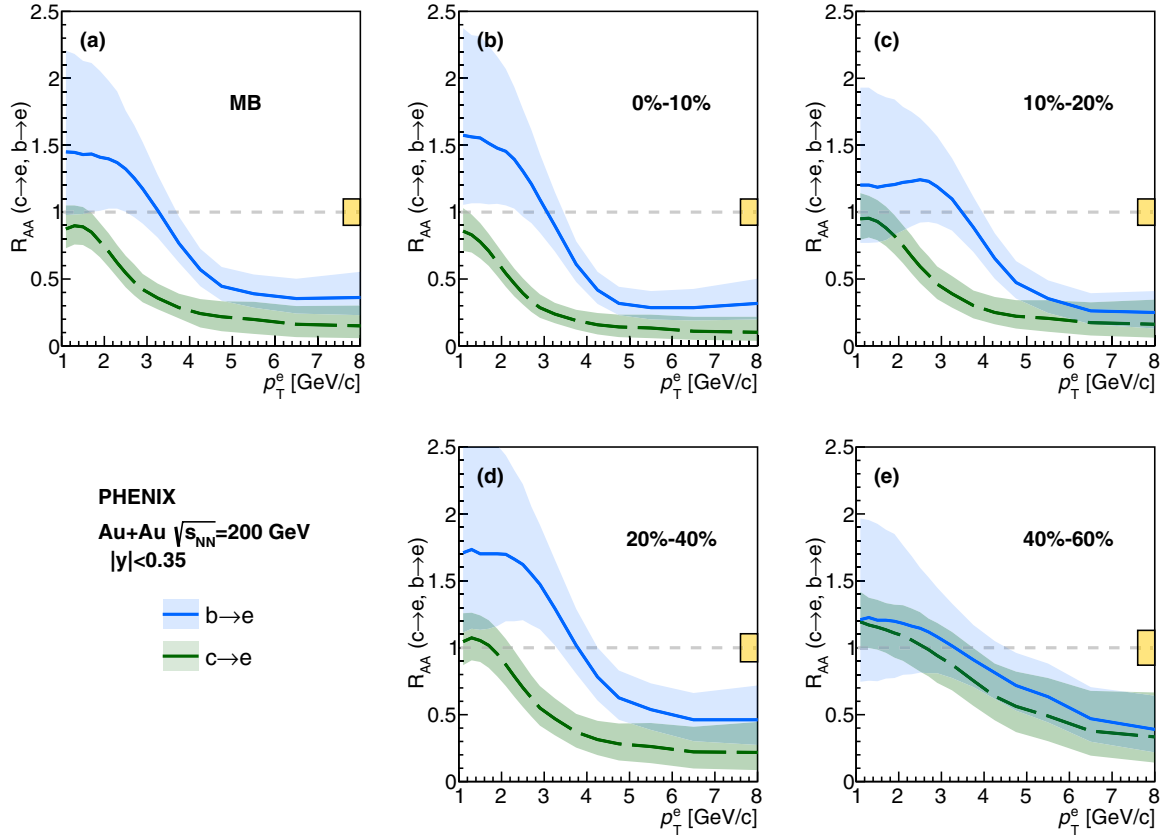


FIG. 13. The nuclear modification of $c \rightarrow e$ and $b \rightarrow e$ as a function of p_T for different centrality classes. The yellow box at unity is the uncertainty on the total normalization.

determining the full probability distribution assuming Gaussian uncertainty on F_{AuAu} , F_{pp} , and R_{AA}^{HF} . The median of the distribution is taken to be the center value with lower and upper one- σ uncertainties of 16% and 84% of the distribution, respectively.

Figure 13 shows $R_{AA}^{c \rightarrow e}$ and $R_{AA}^{b \rightarrow e}$ as a function of p_T for MB Au+Au collisions as well as four centrality classes in Au+Au collisions. These results are improved by six times more Au+Au data than the previous analysis with a wider active area of the VTX detector [12] and the latest $p + p$ [18]. The $p + p$ reference was also improved by using the same VTX analysis technique with ten times more statistics than the previous $p + p$ result [22].

These results extend the p_T coverage down to 1 GeV/c and the systematic bands are reduced by a factor of two. The systematic uncertainty of $R_{AA}^{b \rightarrow e}$ is large at low p_T because of the large uncertainty of F_{pp} at low p_T , but the uncertainty of bottom electrons in Au+Au is independent of p_T . Significant suppression is seen for electrons from both charm and bottom decays at high p_T at MB and all centrality classes. The nuclear modification is consistent with unity within uncertainties at low p_T . Charm electrons show a stronger suppression than bottom electrons for $2 < p_T < 5$ GeV/c in MB and 0%–10%, 10%–20%, 20%–40% centrality classes, whereas charm and bottom suppression are similar at 40%–60%. Note that the prior information used in the unfolding is changed for these centralities. This change can possibly bias the center position

of the resulting $c \rightarrow e$ and $b \rightarrow e$ yields. If there is energy loss, then the p_T spectra are shifted to lower p_T . Therefore, the resulting R_{AA} is suppressed at high p_T , but the yield is slightly enhanced at low p_T to conserve the total number of produced particles. For bottom hadrons, this enhancement can be seen at higher p_T than the charm hadrons due to the harder p_T slope.

The nuclear modification for charm and bottom electrons in 0%–80% Au+Au collisions was reported from the STAR collaboration [9]. As Fig. 14 shows, our unfolding results for charm and bottom electrons are in good agreement with the STAR measurements within uncertainties.

Figure 15 shows the significance of the difference between $R_{AA}^{c \rightarrow e}$ and $R_{AA}^{b \rightarrow e}$, where the ratio of $R_{AA}^{b \rightarrow e}/R_{AA}^{c \rightarrow e}$ is calculated, leading to cancellation of the correlated uncertainty between $c \rightarrow e$ and $b \rightarrow e$ yields. The data show that $R_{AA}^{b \rightarrow e}$ is at least one standard deviation higher than $R_{AA}^{c \rightarrow e}$ in almost the entire p_T range for the most central events 0%–40%, with the largest difference at 3 GeV/c.

To account for possible autocorrelations in the electron-decay kinematics, the R_{AA} of parent charm and bottom hadrons are calculated with the unfolded yield of charm and bottom hadrons as shown in Fig. 16. A significant difference of the yield suppression between charm and bottom hadrons is observed in the region $2 < p_T < 6$ GeV/c in 0%–40% central collisions, similar to what is seen in the decay-electron space.

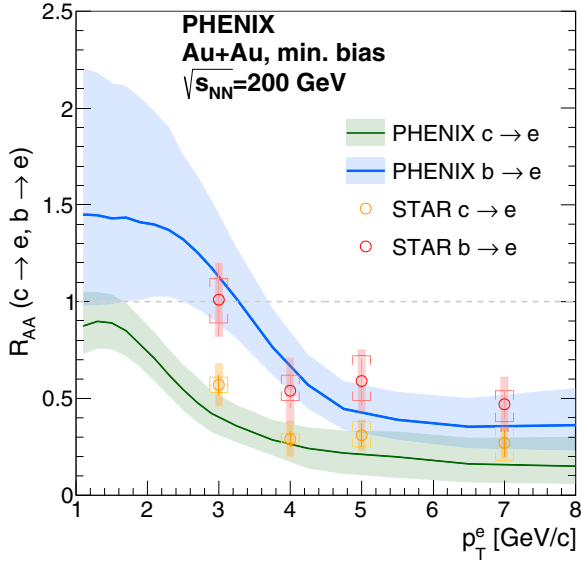


FIG. 14. The nuclear-modification factors of $c \rightarrow e$ and $b \rightarrow e$ as a function of p_T in MB Au+Au Collisions from this work compared with the corresponding measurement from the STAR Collaboration [9].

C. Nuclear modification factor R_{AA} vs. N_{part}

The collision centrality is characterized by the number of nucleon participants in the collision (N_{part}) estimated using Monte Carlo Glauber calculations. The N_{part} -dependent nuclear modifications $R_{AA}^{c \rightarrow e}$ and $R_{AA}^{b \rightarrow e}$ are obtained in three p_T intervals as shown in Fig. 17.

In the low- p_T region (1.0–1.4 GeV/c), there is no N_{part} dependence and no suppression for both $c \rightarrow e$ and $b \rightarrow e$, within uncertainties. The mid- p_T region (2.6–3.0 GeV/c)

shows a clear suppression of charm hadrons when the number of participants increases. The high- p_T region (5.0–7.0 GeV/c) shows an increasing suppression of both charm and bottom hadrons with increasing collision centrality.

D. Comparison to theoretical models

Figure 18 shows a comparison of data to three theoretical models: the T -matrix approach, the SUBATECH model, and the DGLV model. The T -matrix approach is a calculation assuming formation of a hadronic resonance by a heavy quark in the QGP based on lattice quantum chromodynamics [38]. The SUBATECH model employs a hard thermal loop calculation for the collisional energy loss [39]. The DGLV model calculates both the collisional and radiative energy loss assuming an effectively static medium [40]. Because the DGLV model includes only energy loss and does not include the back reaction in the medium, the curves are only shown for $p_T > 5$ GeV/c. All models expect a quark mass ordering for the energy loss in the QGP medium, as observed in the data. The SUBATECH and DGLV calculations for charm suppression agree with the data. The T -matrix approach is slightly higher than the data for $p_T > 3$ GeV/c. The measured bottom nuclear modification is larger than the calculations at $p_T < 4$ GeV/c, although the uncertainty in the measurement is large for $p_T < 2$ GeV/c.

VI. SUMMARY AND CONCLUSIONS

This article reported the results of measurements of the separated invariant yields and nuclear-modification factors of charm and bottom hadron-decay electrons in Au+Au collisions at $\sqrt{s_{NN}} = 200$ GeV at midrapidity. The measurements were performed by the use of a Bayesian unfolding method to extract the invariant yield of parent charm and bottom hadrons

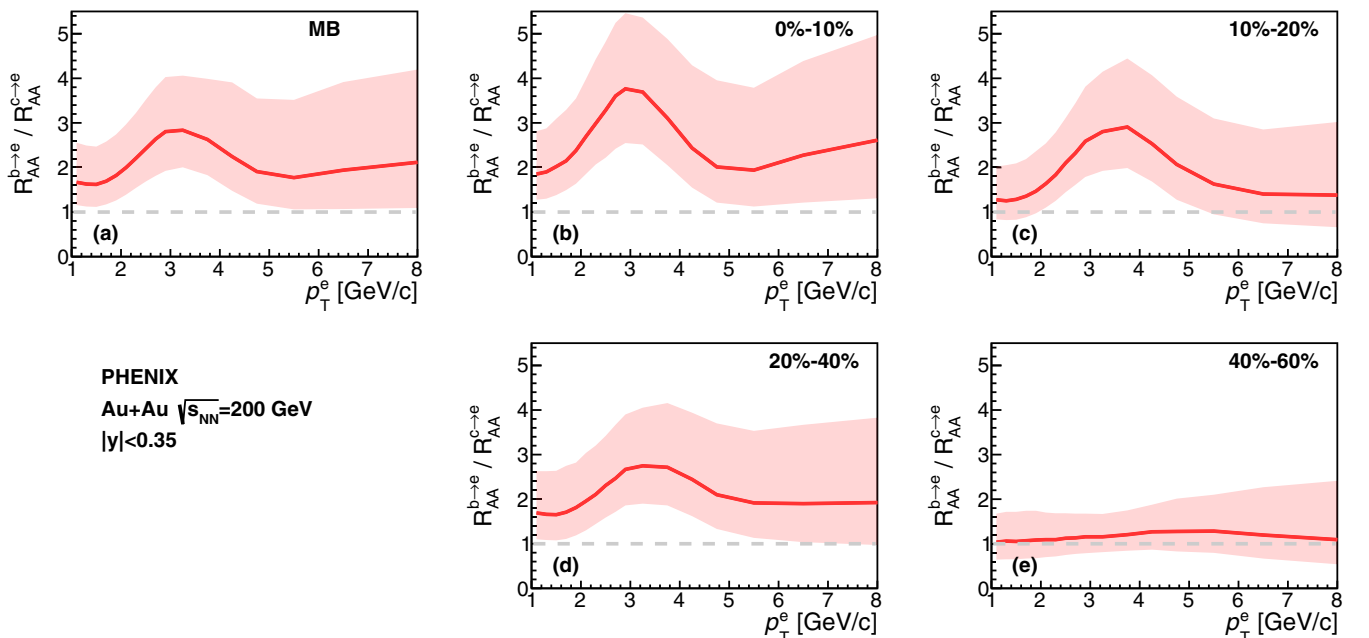


FIG. 15. R_{AA} ratio of $b \rightarrow e$ to $c \rightarrow e$ as a function of p_T for different centrality classes.

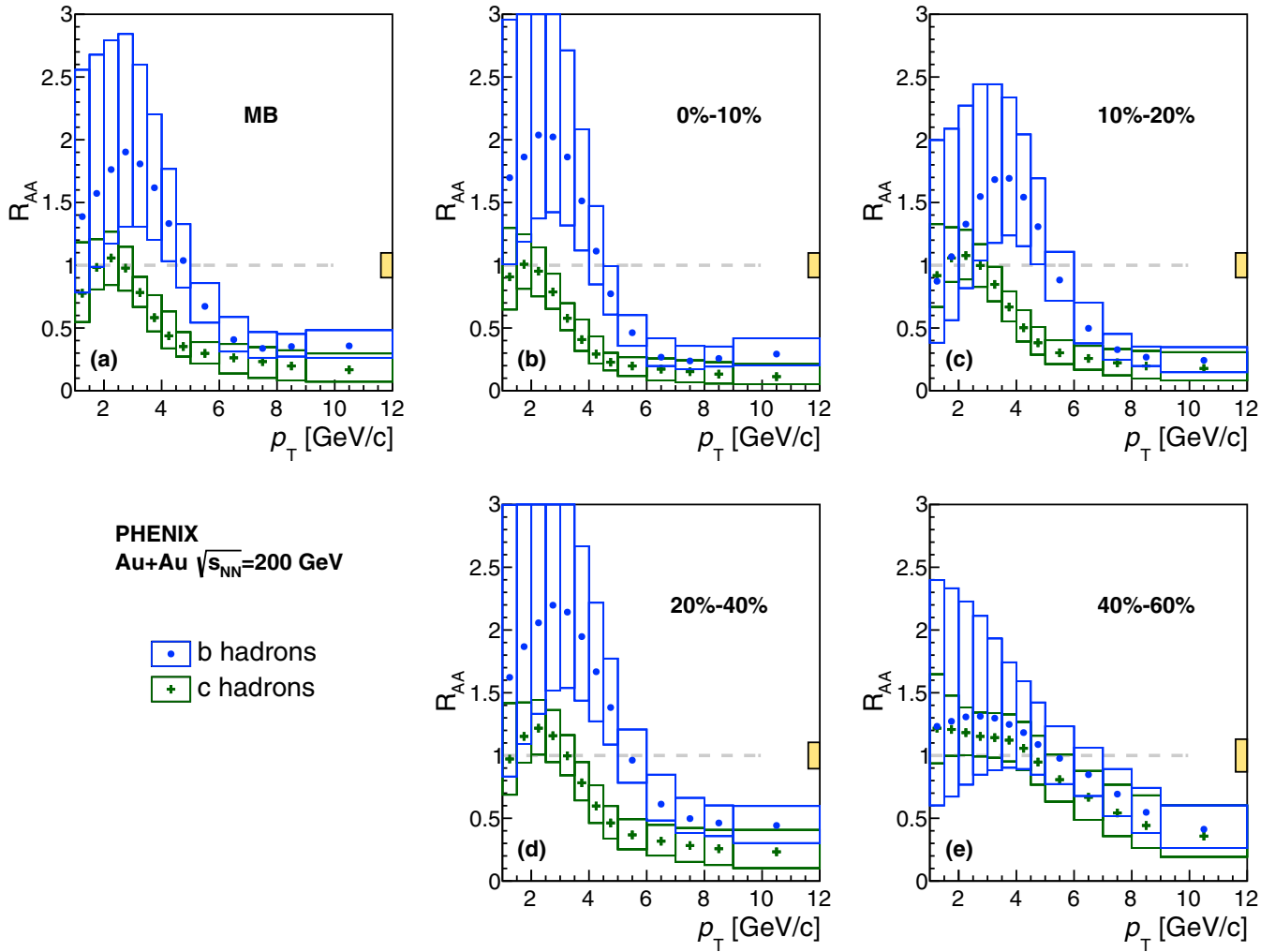


FIG. 16. The nuclear modification of charm and bottom hadrons as a function of p_T for different centrality classes. The yellow box at unity is the uncertainty on the total normalization.

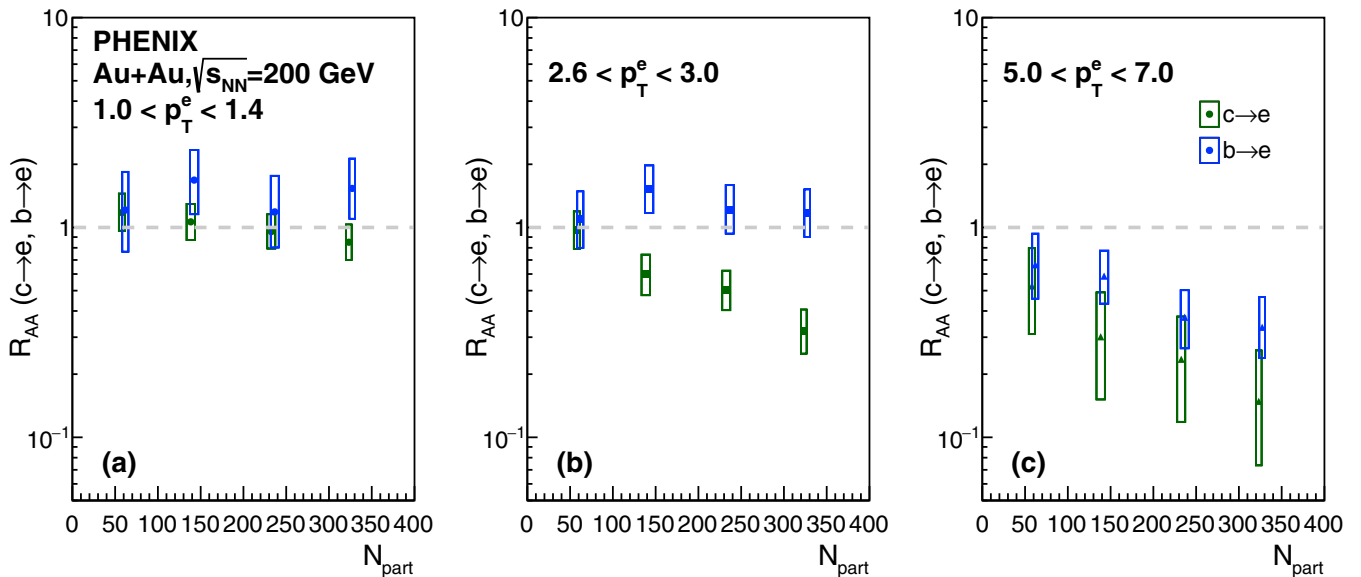


FIG. 17. The R_{AA} for $c \rightarrow e$ and $b \rightarrow e$ as a function of N_{part} in three different p_T ranges. Data points for $c \rightarrow e$ and $b \rightarrow e$ are shifted by -2 and $+2$ from their respective N_{part} for clarity.

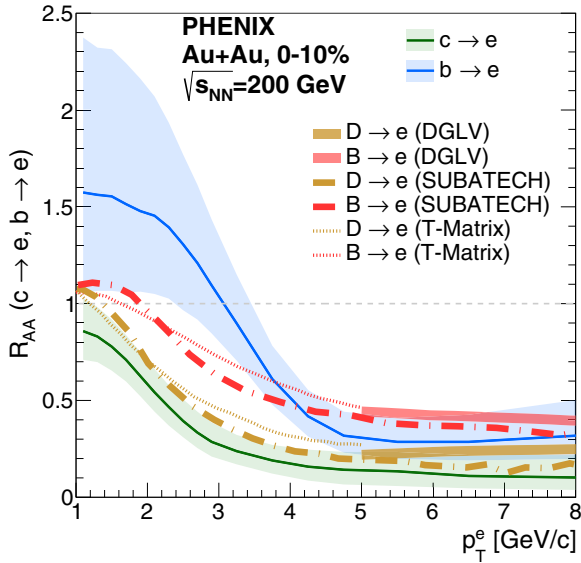


FIG. 18. Measured $R_{AA}^{c \rightarrow e}$ and $R_{AA}^{b \rightarrow e}$ compared to theoretical-model calculations.

from p_T and transverse distance of the closest approach DCA_T distributions of decay electrons.

The nuclear-modification factors R_{AA} have been calculated from the invariant yield in Au+Au and the T_{AA} scaled yield in $p + p$. The comparison between $R_{AA}^{c \rightarrow e}$ and $R_{AA}^{b \rightarrow e}$ indicates that charm hadrons are more suppressed than bottom hadrons by at least one standard deviation for 0%–40% central collisions. Quark-mass ordering of suppression is also seen in the R_{AA} of the parent charm and bottom hadrons, where there is a pattern of R_{AA} consistent with unity for $p_T < 1.4$ GeV/c for both charm and bottom, charm suppression for $2.6 < p_T < 3.0$ GeV/c, and suppression of both charm and bottom for $p_T > 5.0$ GeV/c. These results suggest that charm quarks lose more energy than bottom quarks when crossing the hot and dense medium created in 200 GeV Au+Au collisions in the intermediate- p_T region. The theoretical models used to compare with our data are based on different energy-loss

mechanisms and all agree with the mass ordering and the charm suppression for the entire p_T range covered by this measurement. However, the same models overestimate the bottom-quark suppression in the intermediate p_T region.

ACKNOWLEDGMENTS

We thank the staff of the Collider-Accelerator and Physics Departments at Brookhaven National Laboratory and the staff of the other PHENIX participating institutions for their vital contributions. We acknowledge support from the Office of Nuclear Physics in the Office of Science of the Department of Energy, the National Science Foundation, Abilene Christian University Research Council, Research Foundation of SUNY, and Dean of the College of Arts and Sciences, Vanderbilt University (USA), Ministry of Education, Culture, Sports, Science, and Technology and the Japan Society for the Promotion of Science (Japan), Natural Science Foundation and Ministry of Science and Education (Croatia), Ministry of Education, Youth and Sports (Czech Republic), Centre National de la Recherche Scientifique, Commissariat à l'Énergie Atomique, and Institut National de Physique Nucléaire et de Physique des Particules (France), J. Bolyai Research Scholarship, EFOP, the New National Excellence Program (ÚNKP), NKFIH, and OTKA (Hungary), Department of Atomic Energy and Department of Science and Technology (India), Israel Science Foundation (Israel), Basic Science Research and SRC(CENuM) Programs through NRF funded by the Ministry of Education and the Ministry of Science and ICT (Korea), Ministry of Education and Science, Russian Academy of Sciences, Federal Agency of Atomic Energy (Russia), VR and Wallenberg Foundation (Sweden), University of Zambia, the Government of the Republic of Zambia (Zambia), the U.S. Civilian Research and Development Foundation for the Independent States of the Former Soviet Union, the Hungarian American Enterprise Scholarship Fund, the US-Hungarian Fulbright Foundation, and the US-Israel Binational Science Foundation.

- [1] X. Dong, Y.-J. Lee, and R. Rapp, Open heavy-flavor production in heavy-ion collisions, *Annu. Rev. Nucl. Part. Sci.* **69**, 417 (2019).
- [2] S. Acharya *et al.* (The ALICE Collaboration), Measurement of D^0 , D^+ , D^{*+} and D_s^+ production in Pb–Pb collisions at $\sqrt{s_{NN}} = 5.02$ TeV, *J. High Energy Phys.* **10** (2018) 174.
- [3] A. M. Sirunyan *et al.* (CMS Collaboration), Studies of beauty suppression via nonprompt D^0 mesons in Pb–Pb collisions at $Q^2 = 4\text{GeV}^2$, *Phys. Rev. Lett.* **123**, 022001 (2019).
- [4] A. M. Sirunyan *et al.* (CMS Collaboration), Nuclear modification factor of D^0 mesons in PbPb collisions at $\sqrt{s_{NN}} = 5.02$ TeV, *Phys. Lett. B* **782**, 474 (2018).
- [5] A. M. Sirunyan *et al.* (CMS Collaboration), Measurement of the B^\pm meson nuclear modification factor in Pb–Pb collisions at $\sqrt{s_{NN}} = 5.02$ TeV, *Phys. Rev. Lett.* **119**, 152301 (2017).
- [6] A. M. Sirunyan *et al.* (CMS Collaboration), Measurement of B_s^0 meson production in pp and PbPb collisions at $\sqrt{s_{NN}} = 5.02$ TeV, *Phys. Lett. B* **796**, 168 (2019).
- [7] J. Adam *et al.*, Centrality and transverse momentum dependence of D^0 -meson production at midrapidity in Au+Au collisions at $\sqrt{s_{NN}} = 200$ GeV, *Phys. Rev. C* **99**, 034908 (2019).
- [8] G. Aad *et al.* (ATLAS Collaboration), Measurement of the nuclear modification factor for muons from charm and bottom hadrons in Pb+Pb collisions at 5.02 TeV with the ATLAS detector, *Phys. Lett. B* **829**, 137077 (2022).
- [9] M. S. Abdallah *et al.* (STAR Collaboration), Evidence of mass ordering of charm and bottom quark energy loss in Au+Au collisions at RHIC, *Eur. Phys. J. C* **82**, 1150 (2022); [Erratum: *Eur. Phys. J. C* **83**, 455(E) (2023)].
- [10] S. Acharya *et al.*, Measurement of electrons from semileptonic heavy-flavour hadron decays at midrapidity in pp and Pb–Pb

- collisions at $\sqrt{s_{NN}} = 5.02$ TeV, *Phys. Lett. B* **804**, 135377 (2020).
- [11] M. Aaboud *et al.* (ATLAS Collaboration), Measurement of the suppression and azimuthal anisotropy of muons from heavy-flavor decays in Pb+Pb collisions at $\sqrt{s_{NN}} = 2.76$ TeV with the ATLAS detector, *Phys. Rev. C* **98**, 044905 (2018).
- [12] A. Adare *et al.* (PHENIX Collaboration), Single electron yields from semileptonic charm and bottom hadron decays in Au+Au collisions at $\sqrt{s_{NN}} = 200$ GeV, *Phys. Rev. C* **93**, 034904 (2016).
- [13] M. G. Mustafa, D. Pal, D. K. Srivastava, and M. Thoma, Radiative energy loss of heavy quarks in a quark gluon plasma, *Phys. Lett. B* **428**, 234 (1998).
- [14] Y. L. Dokshitzer and D. E. Kharzeev, Heavy quark colorimetry of QCD matter, *Phys. Lett. B* **519**, 199 (2001).
- [15] A. Meistrenko, A. Peshier, J. Uphoff, and C. Greiner, Collisional energy loss of heavy quarks, *Nucl. Phys. A* **901**, 51 (2013).
- [16] A. Adil and I. Vitev, Collisional dissociation of heavy mesons in dense QCD matter, *Phys. Lett. B* **649**, 139 (2007).
- [17] A. Adare *et al.* (PHENIX Collaboration), Cold-nuclear-matter effects on heavy-quark production in d +Au collisions at $\sqrt{s_{NN}} = 200$ GeV, *Phys. Rev. Lett.* **109**, 242301 (2012).
- [18] C. Aidala *et al.*, Measurement of charm and bottom production from semileptonic hadron decays in $p + p$ collisions at $\sqrt{s_{NN}} = 200$ GeV, *Phys. Rev. D* **99**, 092003 (2019).
- [19] K. Adcox *et al.* (PHENIX Collaboration), PHENIX detector overview, *Nucl. Instrum. Methods Phys. Res. A* **499**, 469 (2003).
- [20] M. Baker *et al.*, Proposal for a silicon vertex tracker (VTX) for the PHENIX Experiment (2004), Report No. BNL-72204-2004, <https://www.bnl.gov/isd/documents/28627.pdf>.
- [21] E. J. Mannel, System electronics and DAQ for the silicon vertex detector upgrade for PHENIX, in *15th IEEE-NPSS Real-Time Conference 2007* (IEEE, Piscataway, NJ, 2007), pp. 1–6.
- [22] A. Adare *et al.* (PHENIX Collaboration), Measurement of bottom versus charm as a function of transverse momentum with electron-hadron correlations in $p + p$ collisions at $\sqrt{s} = 200$ GeV, *Phys. Rev. Lett.* **103**, 082002 (2009).
- [23] S. S. Adler *et al.* (PHENIX Collaboration), Suppressed π^0 production at large transverse momentum in central Au+Au collisions at $\sqrt{s_{NN}} = 200$ GeV, *Phys. Rev. Lett.* **91**, 072301 (2003).
- [24] P. A. Zyla *et al.* (Particle Data Group), Review of particle physics, *Prog. Theo. Exp. Phys.* **2020**, 083C01 (2020), and 2021 update.
- [25] S. S. Adler *et al.* (PHENIX Collaboration), Identified charged particle spectra and yields in Au+Au collisions at $\sqrt{s_{NN}} = 200$ GeV, *Phys. Rev. C* **69**, 034909 (2004).
- [26] A. Adare *et al.* (PHENIX Collaboration), J/ψ production versus centrality, transverse momentum, and rapidity in $\sqrt{s_{NN}} = 200$ GeV, *Phys. Rev. Lett.* **98**, 232301 (2007).
- [27] A. Adare *et al.* (PHENIX Collaboration), Suppression pattern of neutral pions at high transverse momentum in Au+Au collisions at $\sqrt{s_{NN}} = 200$ GeV and constraints on medium transport coefficients, *Phys. Rev. Lett.* **101**, 232301 (2008).
- [28] A. Adare *et al.* (PHENIX Collaboration), Transverse momentum dependence of η meson suppression in Au+Au collisions at $\sqrt{s_{NN}} = 200$ GeV, *Phys. Rev. C* **82**, 011902(R) (2010).
- [29] A. Adare *et al.* (PHENIX Collaboration), Heavy quark production in $p + p$ and energy loss and flow of heavy quarks in Au+Au collisions at $\sqrt{s_{NN}} = 200$ GeV, *Phys. Rev. C* **84**, 044905 (2011).
- [30] D. Foreman-Mackey, D. W. Hogg, D. Lang, and J. Goodman, emcee: The MCMC hammer, *Publ. Astron. Soc. Pac.* **125**, 306 (2013).
- [31] T. Sjöstrand, S. Mrenna, and P. Skands, PYTHIA 6.4 physics and manual, *J. High Energy Phys.* **05** (2006) 026.
- [32] P. Staszal *et al.* (BRAHMS Collaboration), Recent results from the BRAHMS experiment, *Nucl. Phys. A* **774**, 77 (2006).
- [33] J. Adam *et al.* (STAR Collaboration), First measurement of Λ_c baryon production in Au+Au collisions at $\sqrt{s_{NN}} = 200$ GeV, *Phys. Rev. Lett.* **124**, 172301 (2020).
- [34] K. Nagashima, Energy loss of charm and bottom quarks in quark-gluon plasma created in Au+Au collisions at 200 GeV, Ph.D. thesis, Hiroshima University, 2019.
- [35] P. Sorensen and X. Dong, Suppression of nonphotonic electrons from enhancement of charm baryons in heavy ion collisions, *Phys. Rev. C* **74**, 024902 (2006).
- [36] L. Adamczyk *et al.* (STAR Collaboration), Observation of D^0 meson nuclear modifications in Au+Au collisions at $\sqrt{s_{NN}} = 200$ GeV, *Phys. Rev. Lett.* **113**, 142301 (2014); **121**, 229901(E) (2018).
- [37] A. M. Adare, M. P. McCumber, J. L. Nagle, and P. Romatschke, Examination whether heavy quarks carry information on the early-time coupling of the quark-gluon plasma, *Phys. Rev. C* **90**, 024911 (2014).
- [38] H. van Hees, M. Mannarelli, V. Greco, and R. Rapp, Nonperturbative heavy-quark diffusion in the quark-gluon plasma, *Phys. Rev. Lett.* **100**, 192301 (2008).
- [39] P. B. Gossiaux and J. Aichelin, Towards an understanding of the RHIC single electron data, *Phys. Rev. C* **78**, 014904 (2008).
- [40] M. Djordjevic and M. Djordjevic, Heavy flavor puzzle from data measured at the BNL Relativistic Heavy Ion Collider: Analysis of the underlying effects, *Phys. Rev. C* **90**, 034910 (2014).